Highly porous microlattices as ultrathin and efficient impact absorbers

Chang Quan Lai[a,b,*], Chiara Daraio[b]

[a] Temasek Laboratories, Nanyang Technological University, 50 Nanyang Drive 637553, Singapore
[b] California Institute of Technology, 1200 E California Blvd, Pasadena, CA 91125, USA

ARTICLE INFO

The deformation and impact energy absorption properties of ultrathin polymeric microlattices were investigated as a function of density, size and positional eccentricity of the trusses, which controlled the amount of bending in the microlattice deformations. We considered highly porous, 3-D microstructures with small lattice constants ($\leq 135\,\mu m$), and studied their response to high strain rate ($\sim 1000/s$) tests, using high speed video capture, SEM imaging and quantitative modelling. The microlattices were found to have excellent impact absorption efficiencies that are 2 - 120 times better than carbon nanotube foams, polycarbonate and silicone rubber, despite being an order of magnitude slimmer than the thinnest commercial foams of similar densities. This high impact absorption efficiency is largely due to the sideways buckling of the microlattice trusses during the crushing stage, which prevented densification of the microlattices at small strains. Furthermore, we showed that varying the positional eccentricity of the trusses and the number of unit cells in the microlattices can modulate their stiffness, strength and energy absorption over an appreciable range, comparable to that obtained through modifications in relative density. Because the microlattices were mostly under stress equilibrium during the impact process, the insights derived from the present study are expected to be valid for quasistatic and low strain rate loadings as well.

1. Introduction

Shock absorbing materials are critical for the protection of portable computing devices (e.g., laptops, mobile phones and tablets) against accidental collisions and falls. Such commercial applications require protective materials to be thin ($\leq 1\,mm$), both to enable rapid dissipation of the heat generated by on-chip operations and for practical packaging [1,2]. Within the electronic devices, these shock absorbers take the form of gaskets and pads placed around sensitive electronics such as hard disk drives, batteries and cameras [1,2]. Externally, they are often employed as protective cases or skins covering the entire device. As the form factor of mobile computers continue its trend towards slimmer designs, and heat management becomes more difficult with increasingly powerful computer chips and fast battery charging technology [3], there is a strong interest in developing thinner, lighter and more compact shock absorbers.

This goal, however, cannot be easily realized with current materials because of the trade-off between the minimum manufacturable thickness and the impact absorption efficiency, which is the quantity of mass/volume required to dissipate a given amount of impact energy. High porosity foams, for instance, have good impact absorption efficiencies [4–7], but because of the relatively large size and irregular arrangement of the voids within the material, they cannot be made very thin ($< 1\,mm$) without losing uniformity in their mechanical properties (see Supplementary Information). On the other hand, low porosity foams and solid materials such as silicone rubber can be manufactured in very thin sheets ($\sim 20\,\mu m$) [8,9], but they tend to have poor impact absorption efficiencies [10–12] in the range of threshold stresses (0.1 – 10 MPa) for electronics protection [1].

To reconcile small thicknesses with high impact absorption efficiency, architected microstructures with small lattice constants ($\leq 135\,\mu m$) and high porosity ($> 80\%$) are proposed in this study. To date, experimental investigations of such ultrathin microlattices have mainly been focused on lightweight, load bearing applications, typically utilizing the stretch-dominated octet truss design [13–17], while their potential for energy absorbing applications remain largely unexplored. Therefore, the aim of this study is to characterize the mechanical properties and deformation of the microlattices under dynamic loading conditions, and assess their viability as slim and efficient impact absorbers.
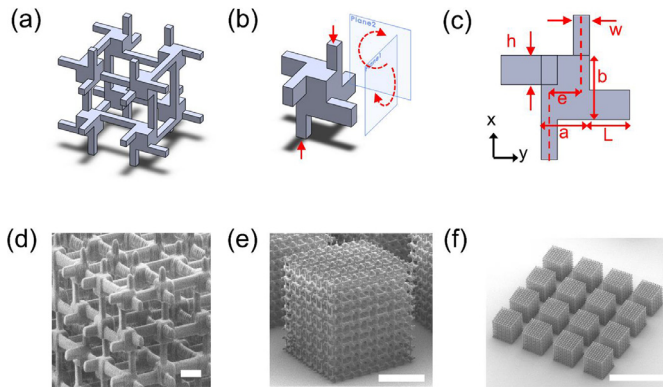
Fig.1. Schematic diagram of (a) a unit cell (b) a sub-unit cell in isometric view and (c) a sub-unit cell in 2 dimensions. SEM images of (d) close-up view of the fabricated unit cells (Scale bar is 10 μm), (e) a single microlattice (Scale bar is 100 μm), (f) a 4 × 4 array of microlattices on a single test sample (Scale bar is 500 μm).

2. Materials and methods

2.1. Microlattice design and fabrication

A unit cell in the microlattice (Fig. 1a) was composed of 8 subunits, each adjacently linked to their mirror images. The subunit (Fig. 1b) consisted of 6 trusses attached to a central cuboid which had dimensions, a (length) x a (width) x b (height) (Fig. 1c). The dimensions of the vertical trusses were L (length) x w (width) x w (height), while that of the horizontal trusses were L (length) x w (width) x h (height) (Fig. 1c). The subunit cells were then assembled into microlattices (Fig. 1d and e). In most experiments, multiple microlattices were placed on a single sample (Fig. 1e) to ensure that the compressive force would be sufficiently large for detection by the piezoelectric sensors during impact testing.

The microlattice geometry described above was chosen because bending deformations of the individual truss elements can be varied systematically using a single geometric parameter, e. This facilitated the analysis of the mechanical response of microlattices with respect to the underlying deformation mechanisms (Fig. 1c). For $e = 0$ μm, the lattice design was essentially simple cubic, and its uniaxial deformation was compression-dominated (i.e., stretch-dominated; see Supplementary Information). For $e > 0$ μm, a uniaxial load generated a rotation of the central cuboid, causing the trusses to bend (Fig. 1b). With increasing e, the bending moment for a given load increased, and therefore, the lattice deformation transitioned from one that was stretch-dominated to one that was bending-dominated. In addition, it can be seen that bending of the horizontal trusses under uniaxial compressive loading would pull the sub-unit cells closer together, shortening the overall width of the microlattice. Therefore, microlattices with $e > 0$ were expected to have a negative Poisson's ratio. Auxetic designs that work on a similar principle had previously been studied in 2-D as well [18,19].

Other than the effect of buckling due to eccentricity (Fig. 2a), we also studied the effects of relative density, by varying the length of the trusses, L (Fig. 2b), and of the relative lattice size, by varying the number of subunit cells, n, along the length of the lattice (Fig. 2c). The relative density, r, refers to the ratio of the lattice density to that of the constituent material, and it is quantitatively equivalent to (1 - porosity). The relative lattice size is determined with respect to the length of the subunit cell, following the convention established in previous studies of stochastic foams, which traditionally characterized the width of gaps in the foams as the cell length [20,21]. The full geometrical details of the fabricated microlattices, measured using SEM images, are given in Table 1.

To fabricate the microlattices, STL files of the models, such as those shown in Fig. 1a–c, were first transferred into a commercial instrument, Photonics Professional GT (Nanoscribe GmbH). Based on the information of these files, the equipment then employed a galvo-mirror system to mechanically position the focal point of an infrared laser at various points within a liquid negative photoresist, IP-Dip (Nanoscribe GmbH), which was deposited on a 2.5 cm × 2.5 cm glass slide. The sections of the negative photoresist that were exposed to this laser focal point then solidified due to 2-photon polymerization, forming the microlattice structures shown in Figs. 1d–f and 2. Unpolymerized photoresist resin was removed through 10 min of isopropyl alcohol immersion, after which the samples were allowed to dry in ambient. The density of cured IP-Dip is 1300 kg/m^3 [13] and the strain-rate dependence of its Young's modulus, E, and yield stress, σ_y, were characterized and reported in the Supplementary Information. For the parameters in this study, E and σ_y were found to be approximately 1.35 ± 0.03 GPa and 76.5 ± 6.5 MPa respectively, which are similar to the quasistatic values reported previously [16].

2.2. Dynamic testing

We performed impact tests on the microlattices using a custom, horizontal impact test setup (Fig. 3) [22–24]. In this system, the microlattices were impacted by a striker that, upon pneumatic activation, slid through a 200 mm long frictionless channel built with air bearings (Newway®). The striker in our tests was made from Delrin polymer ($E = 3.1$ GPa, mass = 10.22 g). The samples were mounted on top of a piezoelectric element (model 200B03, PCB Piezotronics Quartz ICP). The velocity of the striker varied between 0.15 m/s and 0.25 m/s (strain rate = 600/s–1000/s) at the onset of impact.

The striker was fitted with Moire's gratings (pitch = 25 μm) and as it neared the samples, a separate, stationary Moire's gratings on top of the channel created an interference pattern [22–24]. By tracking the intensity of a laser light focused on this interference pattern through an oscilloscope (Tektronix DPO 3034), the distance-time plot of the striker can be obtained. Together with the force-time plot provided by the piezoelectric element which was connected to the same oscilloscope (sampling rate = 10^7/s), the force-distance plot, and consequently, the stress-strain plot for each impact experiment was computed. Because of the small thickness of the samples, the microlattices reached dynamic stress equilibrium very quickly (the ringing-up time was estimated at ∼ 0.2% of the impact duration [5]) and thus, even the elastic, small deformation regime of the impact process could be reliably examined.

Each impact test was also recorded with a high-speed camera, Phantom V12.1 (Vision Research), operated at 8000 fps, exposure time of 105 μs and resolution of 1024 pixels × 768 pixels. The camera was fitted with K2/SC long distance magnifying lenses (Infinity Photo-optical Co.), with a resolution of 2 μm/pixel.

2.3. SEM microscopy

Pristine microlattices and microlattices that were crushed after dynamic testing, were characterized using a Hitachi Nanoshield scanning electron microscope (SEM) at 1 kV. The microlattices were sputtered with a 5 nm thick Pt layer prior to SEM examination, to improve the image quality at high resolution scanning. Due to the Pt coating, pristine microlattices subjected to SEM examination were not used for experimental testing.

3. Results

The raw (light blue) and filtered (dark blue) dynamic stress-strain plots obtained from impact tests on microlattices with varying e, r and n are presented in Fig. 4, Fig. 5 and Fig. 6 respectively. It can be observed that each plot can generally be separated into 4 distinct regimes as indicated in the schematic diagram in Fig. 7a. In stage A, the initial
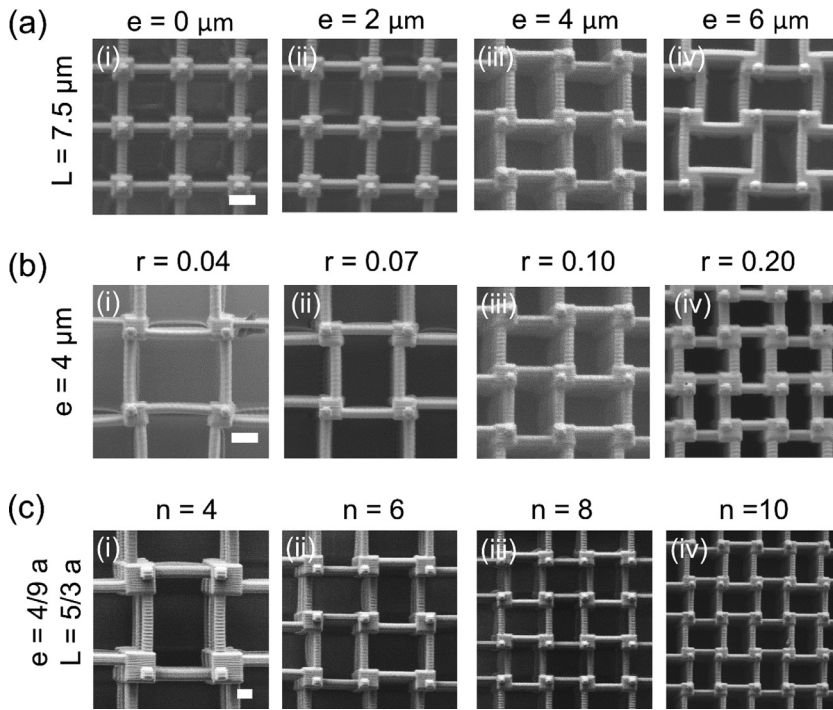
Fig.2. Top view SEM images of microlattices with different (a) positional eccentricity of trusses, *e*, (b) relative density, *r*, (c) relative lattice size. *n* refers to the number of subunit cells making up the length of a microlattice, and was varied by scaling the unit cell size, while keeping the dimensions of the microlattice constant. Scale bars in a(i), b(i) and c(i) are 10 μm.

elastic compressive loading of the microlattice caused the stress to rise until a critical magnitude, σ_{c1}. Stage B begins beyond this critical stress, and is characterized by stress that generally oscillated in a series of sharp humps with increasing strain. In stage C, the densification regime, the stress rose rapidly to a maximum, and in stage D, the stress decreased precipitously as the striker unloads from the microlattice.

These trends resemble the stress-strain plots obtained from quasi-static and dynamic testing of stochastic foams [5,7]. The main difference is that, for stochastic foams, the stress-strain curves usually plateau, rather than oscillate, in stage B. Stress humps similar to the one observed in our lattices, however, were previously reported for compressive tests on cubic lattices [25], and were shown to be caused by the sequential fracture of the lattice struts.

A characteristic feature of the eccentric microlattices (*e* > 0) is their expected auxetic behaviour [18,19]. However, in our impact tests, displays of auxetic behaviour were only found in stage A (Fig. 7b). An examination of the slow-motion video capture revealed that both the stress oscillations and the loss of auxetic deformation were caused by the serial failing of lattice layers (defined in Fig. 8a) adjacent to the substrate or striker boundaries (see Supplementary Video). This can be further confirmed by noting that the number of stress humps in each stress-strain plot matches the number of lattice layers in the respective structures.
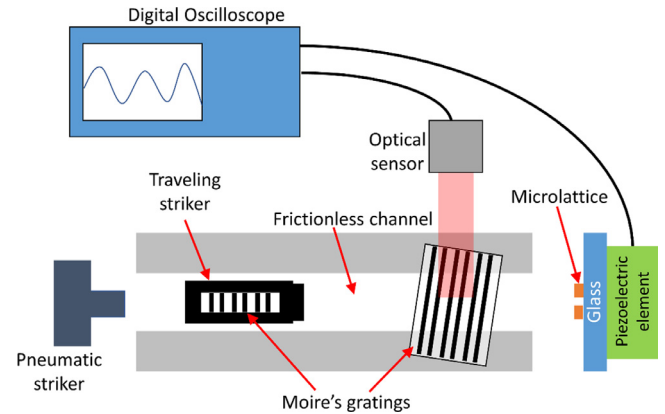

Fig.3. Schematic diagram of the impact test setup.

4. Quantitative analysis

To derive additional insights into the fundamental mechanisms involved in the dynamic deformation of the different microlattice designs, we developed a quantitative model from first principles, using observations made from SEM and high-speed imaging (Figs. 8 and 9).

Table1
Details of microlattice dimensions measured from SEM images.

Fig.	*e* (μm)	*L* (μm)	*a* (μm)	*b* (μm)	*h* (μm)	*w* (μm)	Lattice base area (μm)	Lattice height (μm)	No. of sub-units (base length x base width x height)	No. of lattices on sample	Relative Density (*r*)
2ai	0.0	7.5	9.0	12.0	5.5	3.0	240 × 240	243	10 × 10 × 9	16	0.10
2aii	2.0	7.5	9.0	12.0	5.5	3.0	240 × 240	243	10 × 10 × 9	16	0.10
2aiii/ 2biii/ 2civ	4.0	7.5	9.0	12.0	5.5	3.0	240 × 240	243	10 × 10 × 9	16	0.10
2aiv	6.0	7.5	9.0	12.0	5.5	3.0	240 × 240	243	10 × 10 × 9	16	0.10
2bi	4.0	13	0.0259	9.0	12.0	5.5	228 × 228	228	6 × 6 × 6	49	0.04
2bii	4.0	10	0.0383	9.0	12.0	5.5	232 × 232	224	8 × 8 × 7	36	0.07
2biv	4.0	4.5	0.1140	9.0	12.0	5.5	252 × 252	231	12 × 12 × 11	1	0.20
2ci	10.0	18.8	22.5	30.0	13.8	7.5	270 × 270	270	4 × 4 × 4	16	0.10
2cii	6.7	12.5	15.0	20.0	9.2	5.0	270 × 270	270	6 × 6 × 6	16	0.10
2ciii	5.0	9.4	11.3	15.0	6.9	3.8	270 × 270	270	8 × 8 × 8	16	0.10
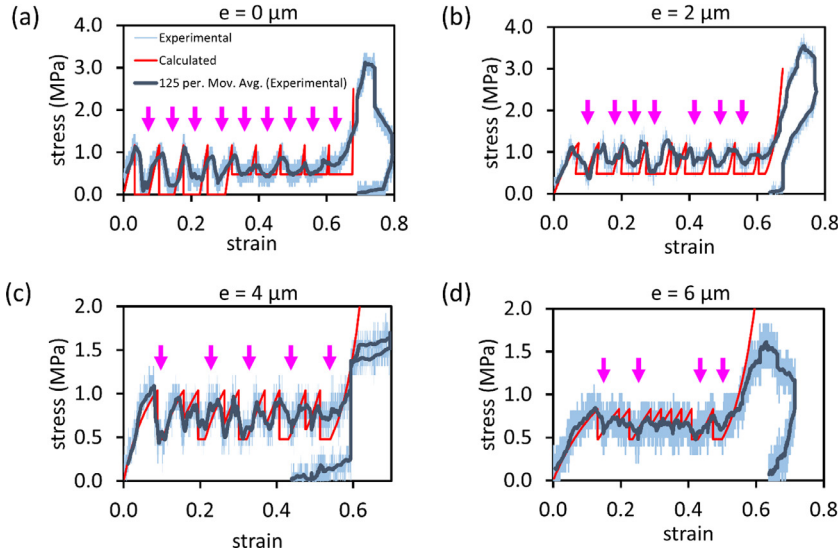
Fig.4. Dynamic engineering stress-strain curves obtained from impact tests conducted on microlattices with different geometrical eccentricity, (a) $e = 0\,\mu m$ (b) $e = 2\,\mu m$ (c) $e = 4\,\mu m$ (d) $e = 6\,\mu m$. The (violet) arrows indicate points where lattice layers were partially or completely fractured. (For interpretation of the references to colour in this figure legend, the reader is referred to the web version of this article.)

Because the microlattices reached stress equilibrium after ∼0.2% of the impact duration, static equations were applied, with suitable substitutions for the strain-rate dependent parameters, such as the Young's modulus, E, and yield stress, σ_y, of the constituent polymer.

4.1. Simple cubic design ($e = 0\,\mu m$)

For $e = 0\,\mu m$ (Fig. 8a), the initial loading of the simple cubic microlattice in stage A ($1 \rightarrow 2$ in Fig. 8a and b) resulted in the compression of the vertical trusses and cuboids, so that the relationship between the compressive stress, σ, and strain, ε, of the lattice can be given by

$$\varepsilon = \frac{\sigma(2L+a)^2}{E(2L+b)}\left(\frac{2L}{w^2} + \frac{b}{a^2}\right). \tag{1}$$

This elastic compressive loading of the vertical trusses and cuboids continued until stress on the vertical trusses reached the critical buckling stress for a beam with fixed ends ($2 \rightarrow 3$, in Fig. 3a and b). The corresponding critical lattice stress for this buckling [26], which can also be considered as the effective lattice failure strength [4], is

$$\sigma_{c1} = \frac{\sigma_Y}{1 + \alpha\left(\frac{L}{g}\right)^2}, \tag{2}$$

where

$$g = \sqrt{\frac{I_v}{w^2}}, \tag{3}$$

I is the second moment of area, the subscript v denotes the vertical truss, and α is a constant that was empirically determined to be approximately $1/3000$, in line with the values obtained from other materials [26].

In Eq. (2), we use the Rankine–Gordon equation in lieu of the Euler buckling relation, as the slenderness ratios of trusses in the microlattices were relatively small (10 - 30). In addition, we observed that failure of the lattice layers consistently took place next to the striker or glass surface, suggesting that the fixed boundary conditions played a role by imposing additional constraints on the microlattice deformation. A complete account of such boundary effects is non-trivial and outside the scope of the current discussion, and therefore, we have opted for a semi-empirical approach in determining σ_{c1} in our analysis.

In the early stages of impact, where the strain rate was high, buckling caused all the vertical trusses in a single lattice layer to fracture simultaneously. This brought the stress to 0 MPa (Figs. 4a and 3 → 5i through dashed line in Fig. 8b) once the critical buckling stress, σ_{c1}, was reached. The lattice stress remained at 0 MPa until the striker travelled the length of the broken lattice layer ($= 2L$) to impact the
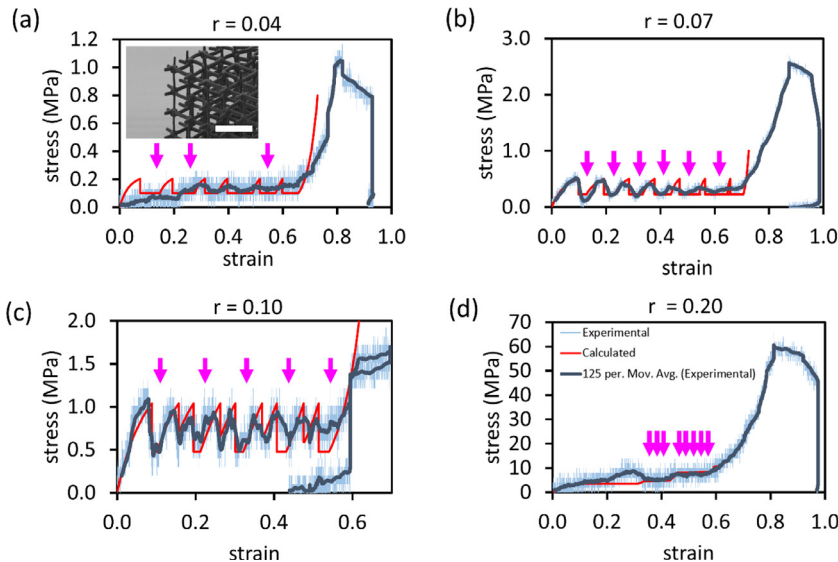

Fig.5. Dynamic engineering stress-strain curves obtained from impact tests conducted on microlattices with different relative density, (a) $r = 0.04$ (b) $r = 0.07$ (c) $r = 0.10$ (d) $r = 0.20$. (inset) SEM image of the microlattice before impact testing. Scale bar is 50 μm. The (violet) arrows indicate points where lattice layers were partially or completely fractured. (For interpretation of the references to colour in this figure legend, the reader is referred to the web version of this article.)
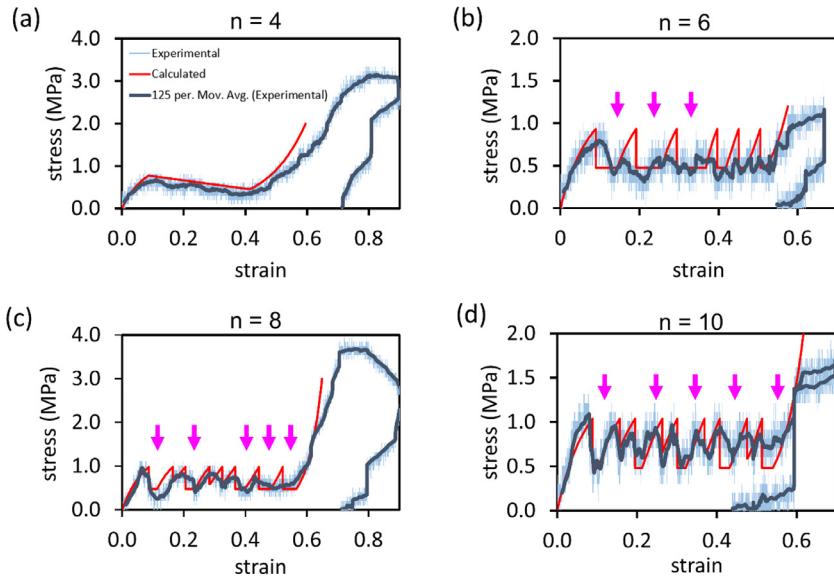
Fig.6. Dynamic engineering stress-strain curves obtained from impact tests conducted on microlattices of different relative lattice size, (a) $n = 4$ (b) $n = 6$ (c) $n = 8$ (d) $n = 10$. The (violet) arrows indicate points where lattice layers were partially or completely fractured. (For interpretation of the references to colour in this figure legend, the reader is referred to the web version of this article.)
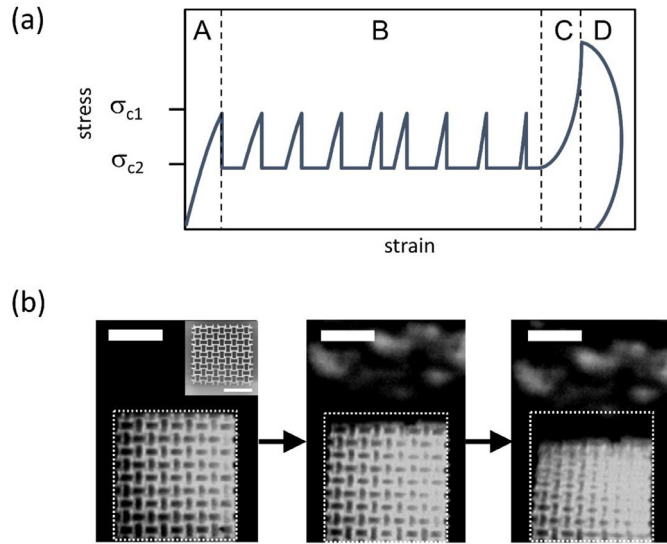
Fig.7. (a) A schematic diagram that describes the general features of the dynamic stress-strain curves. (b) Images from the high-speed video capture showing the auxetic behaviour of microlattice ($e = 6\,\mu m$) during elastic loading from the side view. Scale bars are $100\,\mu m$. (Inset) SEM image of the pristine microlattice from the top view. Scale bar is $100\,\mu m$.

next layer and compress the remaining lattice layers.

In the later stages of impact ($\varepsilon > 0.3$), it was observed that the stress humps became less sharp, and the lattice stress fell to a finite, non-zero value of σ_{c2} after σ_{c1} was reached. This result indicates that the vertical trusses were undergoing significant deformation instead of fracturing simultaneously at the critical buckling stress, which was most likely enabled by the lower strain rates (Supplementary Information). Examination of the slow-motion video confirmed this, showing that the vertical trusses in the boundary layers deformed sideways before collapsing (Fig. 8c). This observation is consistent with the behaviour of similar ductile lattices with 2-D simple cubic geometry under quasi-static mechanical testing [19]. The sideways deformation can be approximated as the buckling of a sliding beam [27], which would take place at the critical lattice stress of

$$\sigma_{c2} = \frac{\sigma_Y}{1 + \alpha\left(\frac{2L}{g}\right)^2}.$$

(4)

The eigenfunction of the deformation shape for the vertical trusses would be approximately $y = \cos(\pi x/2\,L)$, following the coordinates set forth in Fig. 1c. Note that $x = 0$ lies at the interface between the vertical truss and cuboid. Fitting Eq. (4) to the experimental results in Fig. 4a, it was found that α had increased to $1/200$ during the buckling, suggesting that the material properties had changed. This is likely because plastic deformation or fracture was occurring in most of the vertical trusses.

After the lattice stress decreased from σ_{c1} to σ_{c2}, due to the transition between the primary deformation mode ((3) in Fig. 8a) to the
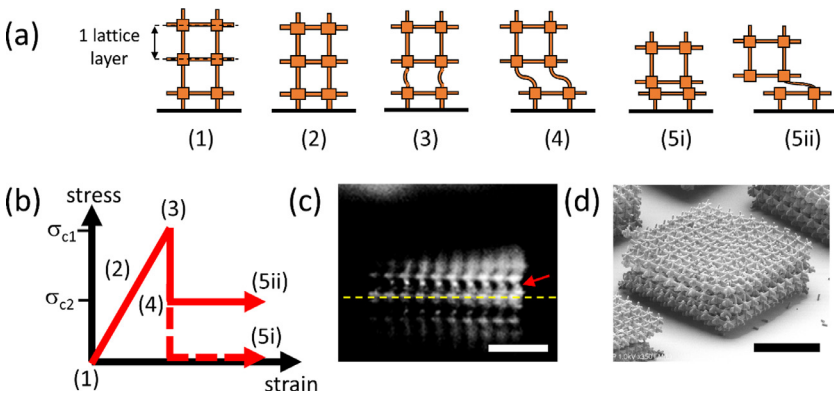
Fig.8. (a) Schematic diagrams illustrating the deformation process and (b) the corresponding lattice stress-strain response for $e = 0\,\mu m$. (c) Single image from the high speed video capture, showing the sideways buckling of the vertical trusses (red arrow) in a microlattice. The yellow dashed line demarcates the boundary between the microlattice and the glass substrate. The reflection of the microlattice can be seen below the line. Scale bar is $100\,\mu m$. (d) SEM image of the microlattice ($e = 0\,\mu m$) after impact testing. Scale bar is $100\,\mu m$. (For interpretation of the references to colour in this figure legend, the reader is referred to the web version of this article.)
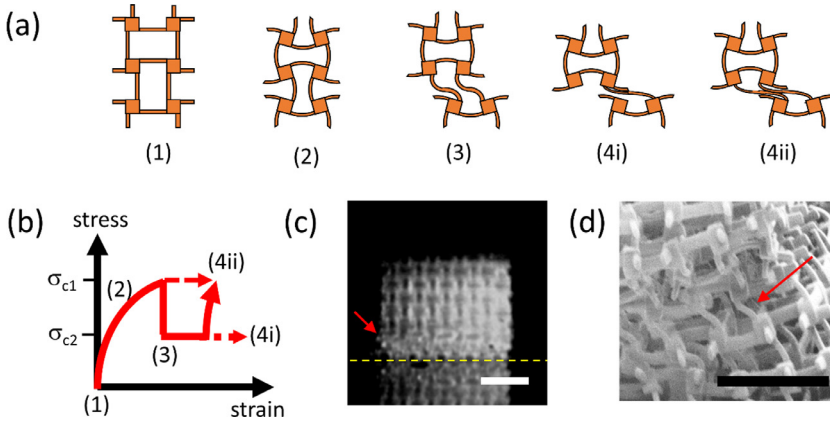
Fig.9. (a) Schematic diagrams illustrating the deformation process and (b) the corresponding lattice stress-strain response for $e > 0\,\mu m$. (c) Single image from high speed video capture showing the sideways buckling of the vertical trusses (red arrow) in a microlattice ($e = 6\,\mu m$). Scale bar is $100\,\mu m$. (d) SEM image of the microlattice ($e = 4\,\mu m$) after impact testing. The red arrow points to the lattice layer displaying the eigenfunction shape of $y = \cos(\pi x / 2L)$. Scale bar is $50\,\mu m$. (For interpretation of the references to colour in this figure legend, the reader is referred to the web version of this article.)

secondary deformation mode ((4) in Fig. 8a), it remained constant at approximately σ_{c2} as the lattice layer continued to buckle further. When snap-through fracture of the trusses in the lattice layer took place Fig. 8d; Supplementary Video), the deformation behaviour transitioned from state ((4) to state (5ii).

All the lattice layers for $e = 0\,\mu m$ were fractured sequentially, until only the cuboids and horizontal trusses of the original microlattices were left (Fig. 8d). Further compression at this point was equivalent to compressing the densified polymer from which the lattices were made. Since this polymer has a much higher stiffness than the microlattice, the stress rose rapidly with strain in Stage C.

4.2. Eccentric designs ($e \geq 0\,\mu m$)

The deformation process for the auxetic microlattice designs (i.e., $e > 0\,\mu m$) was similar to that for the simple cubic microlattices (i.e., $e = 0\,\mu m$). In stage A, onset of the impact load led to elastic loading of the microlattices ($1 \rightarrow 2$ in Fig 9a and b). The buckling deformation of the trusses in this regime was small, and hence, the main contribution to compressive strain of the lattice was the rotation of the central cuboids (Fig. 10a). To quantify this rotation, we first note that both the vertical and horizontal trusses were fixed to the central cuboid, and therefore, the deflection angle at the ends of these trusses must always be the same. Using this constraint, together with static and rotational equilibrium considerations, the stress-strain response of the bending-dominated designs can be found, as detailed in the following.
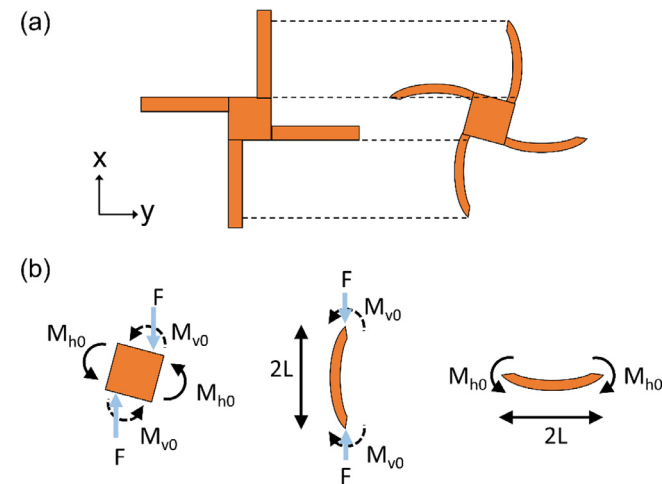
Fig.10. (a) Schematic illustration of how the rotation of the central cuboid increases compressive strain, even when the bent length of the trusses remained unchanged from the original length. (b) Free-body diagrams of the forces and moments acting on the central cuboid, vertical trusses and horizontal trusses.

4.2.1. Small deformations

To derive the 3-D deformation of the eccentric designs, we first consider the 2-D projection of a subunit cell within the bulk of the lattice (Fig. 10). Based on the free body diagrams in Fig. 10b, the equilibrium of moments gives

$$M_{v0} + M_{h0} = \frac{Fe}{2}. \tag{5}$$

Here, F is the force on a single vertical truss and is related to the effective lattice stress, σ, by

$$F = \sigma(2L + a)^2. \tag{6}$$

Using beam theory for the horizontal truss, it can be seen that

$$\theta = \frac{dx}{dy}\bigg|_{y=0} = -\frac{M_{h0}L}{EI_h}, \tag{7}$$

where the subscript h refers to the horizontal truss, θ refers to the rotation of the cuboid in the x-y plane, and $y = 0$ refers to the end of the horizontal truss.

For the vertical truss, the deformation is dictated by the general buckling equation

$$\frac{d^4y}{dx^4} + k^2\frac{d^2y}{dx^2} = 0, \tag{8}$$

where

$$k = \sqrt{\frac{F}{EI_v}}, \tag{9}$$

and the subscript v refers to the vertical truss. Solving Eq. (8) based on the boundary conditions shown in Fig. 10b gives

$$\theta = \frac{dy}{dx}\bigg|_{x=0} = -\frac{M_{v0}}{F}k\tan(kL), \tag{10}$$

for the vertical truss. Note that $0 \leq x \leq 2L$ and $x = 0$ refers to the end of the vertical truss.

Since the rotation of the horizontal truss and vertical truss at the ends, given in Eq. (7) and Eq. (10) respectively, must be the same, and M_{v0} and M_{h0} are also related through Eq. (5), it can be shown that

$$M_{v0} = \frac{F^2eL}{2EI_h k\tan(kL) + 2FL}. \tag{11}$$

Substituting the expression in Eq. (11) into Eq. (10) will then yield the in-plane rotation of the cuboid, θ.

This cuboid rotation drew the ends of the vertical trusses closer (Fig. 10a), and produced a compressive strain. In 3-D, the cuboid would be rotated by θ in the x-y plane, as well as the x-z plane, due to the geometrical symmetry of the microlattices in these planes. The shortening of the distance between the vertical trusses, Δx, can therefore be derived as:
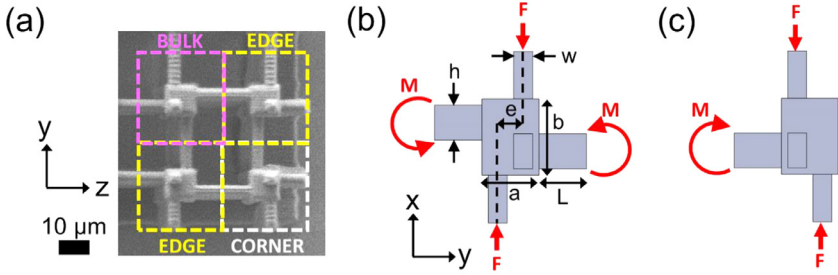
Fig. 11. (a) Magnified SEM image of a microlattice ($n = 8$) from the top view. (b) Schematic illustration of the boundary conditions for a subunit cell with 2 lateral load-bearing trusses in the projected plane. (c) Schematic illustration of the boundary conditions for a subunit cell with 1 lateral load-bearing truss in the projected plane.

$$\Delta x = b(1 - \cos^2\theta) + e\sin\theta(1 + \cos\theta), \tag{12}$$

and the corresponding compressive strain is:

$$\varepsilon = \frac{\Delta x}{2L + b}. \tag{13}$$

4.2.2. Size effects

The analysis in the preceding section pertains only to the bulk subunit cells in the microlattices, which had 4 horizontal load bearing trusses. The edge and corner subunits in a microlattice block, however, have only 3 and 2 of these trusses respectively Fig. 11a). Projecting their geometries onto 2-D planes and considering only load bearing trusses, it can be seen that a bulk subunit cell would have the geometry shown in Fig. 11b in both the x-y and x-z planes, while an edge subunit cell would have the geometry shown in Fig. 11b for only one of the planes, and the geometry shown in Fig. 11c for the other plane. Finally, the corner subunit cell would have the geometry shown in Fig. 11c for both the x-y and x-z planes.

The mechanical equilibrium of the geometry shown in Fig. 11b was previously described in Eqs. (5)–(14). Following the same derivation process for the geometry in Fig. 11c, it can be shown that for the case where only 1 in-plane horizontal truss was bearing load,

$$M_{v0} + \frac{1}{2}M_{h0} = \frac{Fe}{2} \tag{14}$$

and

$$M_{v0} = \frac{F^2 eL}{EI_h k \tan(kL) + 2FL}. \tag{15}$$

Since an edge subunit cell with the 2-D geometry in Fig. 11c was always connected to a bulk subunit cell with the 2-D geometry shown in Fig. 11b, static equilibrium dictates M_{hO} in Eq. (5) and Eq. (17) to be the same, so that

$$\frac{F_{bulk}e}{2} - \frac{F_{bulk}^2 eL}{2EI_h k_{bulk}\tan(k_{bulk}L) + 2F_{bulk}L}$$
$$= F_{edge}e - \frac{2F_{edge}^2 eL}{EI_h k_{edge}\tan(k_{edge}L) + 2F_{edge}L}, \tag{16}$$

where

$$k_{bulk} = \sqrt{\frac{\sigma_{bulk}(2L + a)^2}{EI_v}} \tag{17}$$

and

$$k_{edge} = \sqrt{\frac{\sigma_{edge}(2L + a)^2}{EI_v}}. \tag{18}$$

Similarly, a corner subunit cell with a 2-D geometry in Fig. 11c was always connected to an edge subunit cell with a 2-D geometry in Fig. 11b and hence,

$$\frac{F_{edge}e}{2} - \frac{F_{edge}^2 eL}{2EI_h k_{edge}\tan(k_{edge}L) + 2F_{edge}L}$$
$$= F_{edge}e - \frac{2F_{corner}^2 eL}{EI_h k_{corner}\tan(k_{corner}L) + 2F_{corner}L}, \tag{19}$$

where

$$k_{corner} = \sqrt{\frac{\sigma_{corner}(2L + a)^2}{EI_v}}. \tag{20}$$

Rearranging Eqs. (19) and (22), and using Eq. (6) to relate the force on the vertical truss to the nominal stress, it can then be shown that

$$\sigma_{edge} = \left\{ 2(2L + a)^2 \left[\frac{1}{\sigma_{bulk}(2L + a)^2} + \frac{L}{EI_h}\left(\frac{1}{k_{bulk}\tan(k_{bulk}L)}, \right.\right.\right.$$
$$\left.\left.\left. - \frac{1}{k_{edge}\tan(k_{edge}L)} \right) \right] \right\}^{-1} \tag{21}$$

$$\sigma_{corner} = \left\{ 2(2L + a)^2 \left[\frac{1}{\sigma_{edge}(2L + a)^2} + \frac{L}{EI_h}\left(\frac{1}{k_{edge}\tan(k_{edge}L)}. \right.\right.\right.$$
$$\left.\left.\left. - \frac{1}{k_{corner}\tan(k_{corner}L)} \right) \right] \right\}^{-1} \tag{22}$$

Evaluating Eqs. (21) and (22), it can be observed that $\sigma_{corner} < \sigma_{edge} < \sigma_{bulk}$. This is expected, as a subunit cell with less horizontal trusses to restrict the rotation of the cuboid means that it is less stiff and therefore, contributes less to load bearing.

The overall stress–strain (σ-ε) relationship for the microlattice, after accounting for size effects, can finally be obtained as

$$\sigma = \frac{4}{n^2}\sigma_{corner} + \frac{4(n - 2)}{n^2}\sigma_{edge} + \frac{(n - 2)^2}{n^2}\sigma_{bulk} \tag{23}$$

and

$$\varepsilon = \frac{\sigma_{bulk}(2L + a)^2}{E(2L + b)}\left(\frac{2L}{w^2} + \frac{b}{a^2} \right) + \frac{\Delta x}{2L + b} \qquad \text{for } e < w, \tag{24}$$

and

$$\varepsilon = \frac{\Delta x}{2L + b} \qquad \text{for } e \geq w. \tag{25}$$

The expression for Δx can be found in Eq. (12), and

$$\theta = \frac{\sigma_{bulk} eL k_{bulk}(2L + a)^2 \tan(k_{bulk}L)}{2EI_h k_{bulk}\tan(k_{bulk}L) + 2\sigma_{bulk}L(2L + a)^2}. \tag{26}$$

Eqs. (24) and (25) take into consideration that geometries with $e < w$ would be subjected to both compressive and bending strains, due to the overlap of cross-sectional area of trusses on opposite sides of the central cuboid, while geometries with $e \geq w$ would only be subjected to the bending strain. From Eq. (23), it can be observed that as n approaches ∞ (i.e., lattices with very large overall dimensions), the lattice stress, σ, approaches σ_{bulk}, which is expected, as the bulk subunits would vastly outnumber the edge and corner subunits, and the mechanical properties of the microlattice would depend only on the geometry of the

bulk subunits (i.e., no size effects). In such cases, the analysis in the preceding section would be sufficient to derive the stress-strain relationship of these lattices.

4.2.3. Failure

The elastic loading of the microlattices would continue until plastic deformation occurred in the vertical trusses, specifically, when the surface bending stress of the vertical trusses in a bulk subunit cell exceeded σ_y for $0.25\,(2L) \leq x \leq 0.75\,(2L)$, where $2L$ is the length of the vertical trusses in a lattice layer. Failure is expected to occur in the vertical trusses of the bulk subunit cell as they bear more stress than the edge and corner subunit cells. The above criterion was determined through semi-empirical fitting and was consistent across all the samples. Similar to the analysis performed for the simple cubic case ($e = 0$ μm), it also incorporates the influence of the fixed boundary conditions imposed on the microlattices by the hard striker and substrate surfaces. Quantitatively, the critical bulk lattice stress, $\sigma_{c1,b}$, that brought about this instability can be expressed as

$$\sigma_y = \frac{M_{c1}w}{2I_v}, \tag{27}$$

where

$$M_{c1} = \frac{eEI_v k_{c1,b}{}^2 \sigma_{c1,b} L(2L + a)^2}{2EI_h k_{c1,b}\tan(k_{c1,b}L) + 2\sigma_{c1,b}L(2L + a)^2}\left[\tan(k_{c1,b}L)\sin\left(\frac{k_{c1,b}L}{2}\right)\right.$$
$$\left. + \cos\left(\frac{k_{c1,b}L}{2}\right)\right], \tag{28}$$

$$k_{c1,b} = \sqrt{\frac{\sigma_{c1,b}(2L + a)^2}{EI_v}}. \tag{29}$$

Substituting σ_{bulk} with $\sigma_{c1,b}$ in Eqs. (23)–(26), the corresponding lattice stress for failure, σ_{c1}, and the strain at which it occurred, can then be computed.

Like in the case of simple cubic microlattices, the onset of plastic deformation in the trusses led to instability and subsequently, a transition from the primary deformation mode to the secondary deformation mode (2→3 in Figs. 9a and b, Figs. 9c and Fig. d). During this process, the stress on the microlattice fell from σ_{c1} to σ_{c2}, which was given in Eq. (4). For $L = 4.5$ μm, however, this decrease was not observed (Fig. 5d), most likely because the short truss length led to snap-through buckling (2→4ii in Fig. 9a and b).

After the transition to the secondary deformation mode, snap-through fracture could occur in the lattice layers, like in the case for the simple cubic geometry, and the lattice stress stayed approximately constant at σ_{c2} until the striker reached the next lattice layer (3 → 4i through the dotted line in Fig. 9b). In the event the trusses did not fracture, they continued to bear load and the stress-strain relationship of the lattice layer can then be described by large deformation calculations in the secondary buckling mode (3 → 4i through the dotted line in Fig. 9b). These computations were performed numerically with the Galerkin's method of weighted residual (Supplementary Information), using the secondary deformation shape as trial function,

$$y(x) = q\cos\left(\frac{\pi x}{2L}\right). \tag{30}$$

The above deformation processes then repeat until all the lattice layers in the auxetic microlattices had been compacted, and densification of the remaining cuboids and crushed trusses occurred in stage C.

4.3. Comparison of quantitative model with experimental results

To validate the above analysis, the quantitative model was compared to the experimental data in Figs.4–6 (calculated plots in red). No fitting parameters were used in the derivation of the theoretical plots, other than in Eqs. (4) and (27) for computing the critical failure

stresses. Despite this, it can be observed that there is good agreement between the theory and experimental results, indicating that the deformation mechanisms discussed above provided a reasonably accurate depiction of the microlattice crushing process. Since the quantitative model was based on static equations, the analysis can also be extended to describe quasi-static loads, as long as the appropriate values are used for strain-rate dependent material parameters, such as E and σ_y.

By matching the strains of the calculated stress humps in stage B and the onset of densification to the experimental plots, the lattice layers that fractured could be identified individually (indicated with violet arrows in Figs.4–6). It can be observed that the proportion of fractured lattice layers decreased with increasing e (Fig. 4a–d), but remained approximately constant at 50% for microlattices with different r and n but the same e. Clearly, lattice designs that introduce greater bending reduce the probability of trusses fracturing. One possible reason for this could be because vertical trusses in such designs had already been subjected to limited bending deformation during the elastic loading stage and thus, the transition to the secondary deformation mode for these trusses was more gradual than that for the simple cubic design.

Despite the general agreement of the quantitative model with the experimental results, there were two significant deviations. First, the quantitative model overestimated the lattice stress for $r = 0.04$ during the elastic loading phase in Stage A (Fig. 5a), which can be attributed to fabrication defects in the lattice trusses. As can be seen from the inset of Fig. 5a, some of the vertical trusses of the microlattice were not perfectly straight and aligned due to uneven polymer shrinkage along the slender structures during the fabrication process. This, in turn, caused the microlattice to buckle more easily initially.

Second, it was noted that for $n = 6$ (Fig. 6b), $n = 8$ (Fig. 6c) and $n = 10$ (Fig. 6d), the final 4 stress humps, which correspond to the mechanical behaviour of the last 4 lattice layers as they were being crushed, did not reach the expected maximum of σ_{c1}. Instead, they had broad, relatively indistinct peaks compared to the earlier stress humps. Similarly, for the case of $n = 4$ (Fig. 6a), where the pristine microlattice started with only 4 lattice layers, there was no distinct stress peaks found in Stage B. These results suggest that significant plasticity and parallel deformation were involved in the crushing of the final 4 lattice layers. The validity of this postulation was further confirmed by the good agreement obtained between the experimental results for the case of $n = 4$, and calculations based on the parallel, plastic deformation of the lattice layers (Fig. 6a).

To account for this deviation, it should first be noted that the transition of a failing lattice layer from the primary deformation mode to the secondary mode involved lateral deflections. Because the position of the microlattice was fixed at the boundaries, the remaining lattice layers had to deflect horizontally in the opposite direction to accommodate this lateral deformation. If there were many non-failing lattice layers, such as in the early stages for $n = 10$ ("Layer-by-layer crushing" in Fig. 12), then each lattice layer only had to deform slightly, so that they largely retained their elasticity and stayed in the primary deformation mode shape. These lattice layers were, therefore, able to withstand a lattice stress up to σ_{c1} in the subsequent stages of the crushing process.

However, as the number of non-failing lattice layers decreased, either due to a small n in the initial design or successive crushing of lattice layers, the lateral deflection of each of the remaining lattice layers had to correspondingly increase ("Parallel crushing" in Fig. 12). For instance, if there were only 4 non-failing lattice layers, each of these lattice layers would have to deflect laterally up to a displacement of $2L/4$, as the maximum horizontal deflection for the failing lattice layer was ~$2L$ in the secondary buckling mode. Assuming an eigenshape of $y = \cos(\pi x/2L)$ for the sideways deflection of the lattice layers, this would lead to plastic deformation on the surface of the vertical trusses for $0 \leq x \leq 0.3(2L)$ and $0.7(2L) \leq x \leq 2L$. Therefore, the remaining 4 lattice layers would become permanently deflected sideways, in the secondary deformation mode shape. This, together with the lowering of
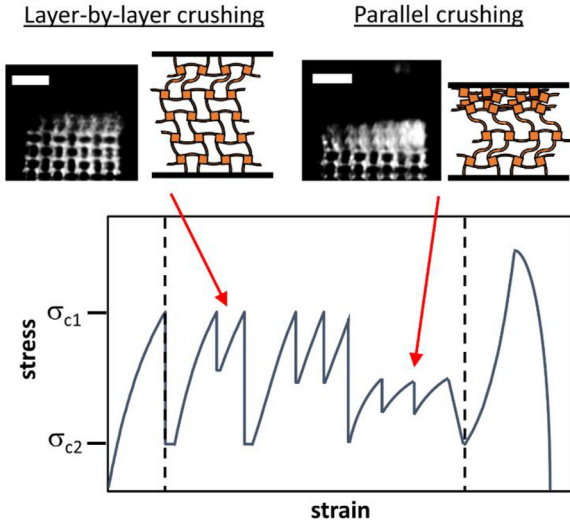
Layer-by-layer crushing

Parallel crushing

Fig.12. Schematic diagram describing the effect of secondary deformation on the failure strength of the lattice layers, accompanied by corresponding high speed camera images. Scale bar is 100 μm.

material stiffness due to plasticity, reduced the maximum failing stress of the microlattice to levels below σ_{c1} for the final lattice layers.

5. Discussion

Besides providing insights into the deformation mechanisms of the impact process, the quantitative model developed in Section 4 can also be employed to predict key mechanical properties of the microlattices based on the geometrical parameters.

5.1. Effect of bending due to the positional eccentricity of trusses

The stiffness, k, failure stress, σ_{c1}, and energy absorbed per unit nominal volume, Q, for microlattices with varying e are plotted in Fig. 13a–c. The experimental data can be observed to follow the calculated trends (dashed lines) closely. As expected, an increase in e induced a greater bending moment on the central cuboid, causing it to rotate more for a given load, resulting in a decrease in microlattice stiffness. In addition, a higher e also resulted in a decrease in σ_{c1} for the microlattices, as excessive bending at high eccentricities would cause the trusses to reach plastic yield at smaller loads.

However, the energy absorbed per unit nominal volume of the microlattices, Q, which can be quantified using the area under the stress-strain curve, has a less straightforward relationship with e. As e increased, the maximum energy that was absorbed by the microlattices was observed to rise initially before decreasing for $e > 2$ μm, so that the energy absorption characteristics for $e = 0$ μm and $e = 4$ μm were nearly identical. This indirect relationship can be attributed to the opposing effects that increasing e has on Q. On the one hand, a higher e causes a decrease in stiffness and failure strength of the microlattices, which lowers Q, but at the same time, it reduces the probability of the

trusses fracturing, so that they continue to deform and absorb more impact energy, leading to an increase in Q.

Two important observations can be derived from the results in Fig. 13. First, for the geometries presented here, the energy absorbed for the stretch-dominated design ($e = 0$) was comparable to that for the bending-dominated design ($e > 0$ μm) (Fig. 13c), which goes against the conventional expectation that stretch-dominated lattice designs have inferior energy absorption capabilities compared to bending-dominated lattice designs [4]. The main reason for this is because the stretch-dominated and bending-dominated geometries in the present study both share the same secondary deformation mechanism, and therefore, have similar energy absorption characteristics.

Second, slight modifications to the simple cubic geometry can bring about appreciable changes in the mechanical properties of the microlattices without altering the relative density. To illustrate this, a best fit line that runs through the shoulder of each energy absorption curve in Fig. 13c, which represents the point of highest impact absorption efficiency for a given e, can be plotted and shown to have a slope of 1.1. This value is comparable to that ($= 1$) obtained through variations in the relative density of ductile foams [7].

5.2. Effect of relative density

Fig. 14a–c show the plots of k, σ_{c1} and Q against r. Both the experimental and calculated plots show that the stiffness and failure strength of the microlattices are related to the relative density by a power law, with exponents of 1.57 and 1.70 respectively. These values are reasonably close to the values of 2 and 1.5 predicted in generalized models [4]. Similarly, the line that represents the points of maximum impact absorption efficiency (dotted line in Fig. 14c) for these microlattices had a slope of 0.99, which is nearly identical to the expected value of 1 for bending-dominated lattices that fail by yielding [7]. Therefore, the changes in the mechanical behaviour of the microlattices in response to a variation in r is in line with that of stochastic foams and other bending-dominated designs.

5.3. Effect of relative lattice size

The effect of relative lattice size, n, on the relative microlattice stiffness, k/k_{bulk}, and the relative failure strength, $\sigma_{c1}/\sigma_{c1,b}$ in the elastic deformation stage are shown in Fig. 15a and Fig. 15b respectively. k/k_{bulk} and $\sigma_{c1}/\sigma_{c1,b}$ have a logarithmic relationship with n as a direct result of the expression in Eq. (23), which expects that the mechanical stiffness and strength of a microlattice to approach that of the bulk at large n, but weaken rapidly as n decreases, due to the increasing influence of the softer edge and corner subunit cells. As a result, the maximum amount of impact energy that can be absorbed in the crushing phase increases with n (Fig. 15c).

The trends shown in Fig. 15a and b are similar to those exhibited by other bending dominated designs due to size effects, such as hexagonal cell geometries [20,21,28]. The main difference, however, is that the aluminium foams with these cell morphologies are significantly less sensitive to n, with the mechanical properties of the lattices attaining bulk values for $n \geq 5$ [20,21,28]. On the other hand, the microlattices
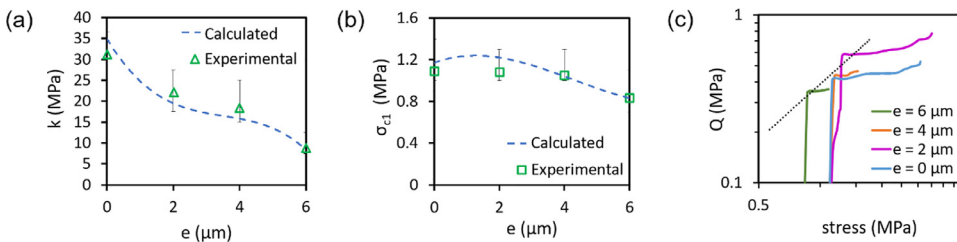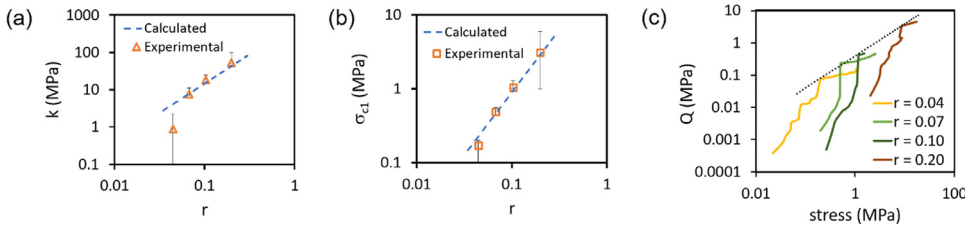

Fig.13. (a) Experimental data points and calculated trend line (dashed line) of effective lattice stiffness, k, as a function of eccentricity, e. (b) Experimental data points and calculated trend line (dashed line) of σ_{c1} vs. e. Error bars in (a) and (b) represent the uncertainty due to noise in the measurements. (c) Experimental plot of energy absorbed per unit volume, Q, against nominal stress for microlattices with different e. The dotted line represents the points where maximum impact absorption efficiency can be achieved.

Fig.14. (a) Experimental data points and calculated trend line (dashed line) of k vs. r. (b) Experimental data points and calculated trend line (dashed line) of σ_{c1} vs. r. Error bars in (a) and (b) represent the uncertainty due to noise in the measurements. (c) Experimental plot of energy absorbed per unit volume, Q, against nominal stress for microlattices with different r. The dotted line represents the points where maximum impact absorption efficiency can be achieved.

achieved.

exhibited only 60% to 80% of the bulk mechanical properties for $4 \leq n \leq 10$ (Fig. 15a and b), indicating that a finer gradation of mechanical characteristics can be achieved at constant relative density, by exploiting size effects for the bending dominated designs based on the simple cubic system.

Furthermore, the maximum impact absorption efficiency line in Fig. 15c can be shown to have a gradient of 1.2, implying that variations in n can bring about a more effective alteration of the energy absorption characteristics of the present microlattice designs than changes in the relative density, r (Fig. 13c). This result is in sharp contrast to previous reports on the dynamic energy absorption of stochastic foams, which displayed little to no size effects [29,30].

5.4. Impact absorption efficiency

The performance of the microlattices as ultrathin and efficient shock absorbers were compared with alternative materials that are commonly used as impact protectors. Since mechanical properties are strain-rate sensitive, only data from similar loading conditions (strain rate ~ 1000/s) were included.
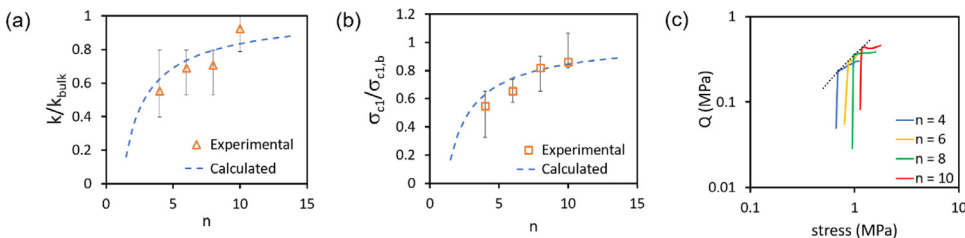
To assess the shock absorption efficiency of the microlattices, the cushion factor [7,23,23,31,32], C, was used as the figure of merit. It is given by

$$C = \frac{\sigma}{Q}, \tag{31}$$

where Q refers to the amount of impact energy absorbed per unit nominal volume of the material for a given stress, σ. Q can be quantified by computing the area under the stress-strain curve up to a given stress, σ. From Eq. (31), it can be seen that a material with a lower cushion factor is more efficient, as it will require less volume to absorb the same amount of impact energy at a given threshold stress. Since C is not a fixed value, but is dependent on σ, we will focus only on the minimum value of the cushion factor, C_{min}, as it represents the maximum impact absorption efficiency of the material.

From Fig. 16a, it can be seen that the maximum impact absorption efficiencies of the microlattices ($C_{min} = 2.53 \pm 0.22$) approached the theoretical limit of $C_{min} = 1$. Furthermore, they were several times better than advanced carbon nanotube foams ($C_{min} = 4.64 - 10.2$) or solid materials, such as silicone rubber ($C_{min} = 5.2 - 6.1$), and were comparable with that of the best foams currently available ($C_{min} = 2.47 \pm 0.39$).

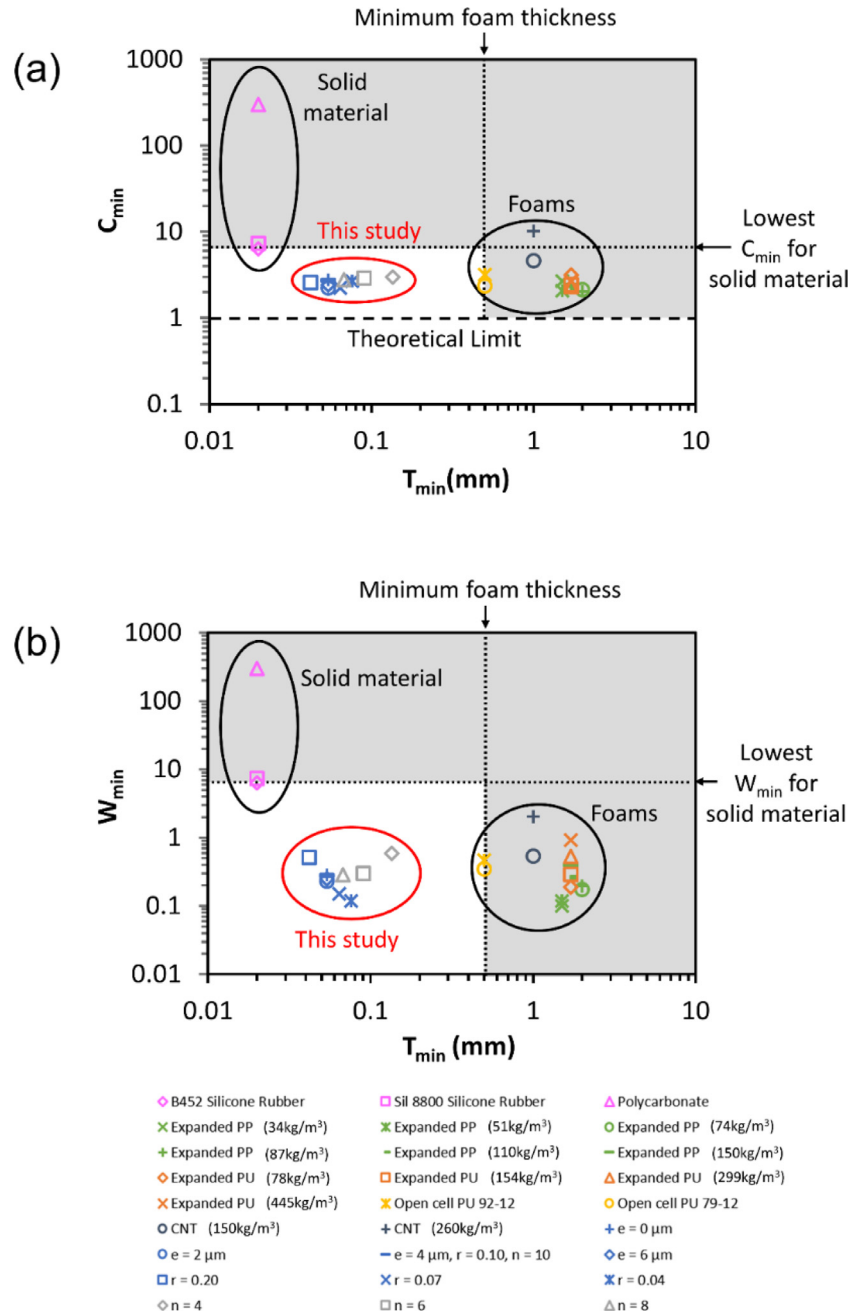Interestingly, the auxetic design of the bending-dominated

microlattices did not increase the values of C_{min} over the simple cubic lattice, even though their negative Poisson's ratios tend to draw material inwards and cause densification at low strains. This is because, at large strains, the deformation of the microlattices shifted from the primary auxetic mode to one that involved the sideways buckling of the lattice layers, thus allowing the microlattices to be compressed to high strains (>0.5) without exceeding the peak stress, σ_{c1}, in the crushing stage. This deformation transition was most important for $r = 0.04$ and $r = 0.07$, which achieved the highest densification strains (~ 0.7) and, consequently, the lowest C_{min} values amongst the microlattices tested in this study.

The main motivation for using microlattices as ultrathin impact absorbers over conventional foams is highlighted in Fig. 16a. It can be observed that, despite comparable C_{min}, the minimum manufacturable thickness, T_{min}, of the microlattices is 3.7 to 11.9 times smaller than the thinnest foams currently available. In addition, solid materials displayed poor impact absorption efficiencies that are 3 to 120 times worse than that of microlattices in the threshold stress range of electronics (1 – 10 MPa), despite the fact that they can be fabricated in ultrathin layers.

Besides nominal volume, the impact absorption efficiency of the microlattice designs were also evaluated with respect to the actual volume of material present in the microstructures by using the index of measure, W_{min}, which can be quantified by multiplying C_{min} with r. Similar to C_{min}, a design with lower W_{min} requires less actual material to absorb the same amount of impact energy at a given stress, i.e., the design makes use of its available material more efficiently for impact absorption. For a given material, such a design would also offer the lowest mass for the same impact absorption performance.

Plotting W_{min} against T_{min} in Fig. 16b, it was found that the microlattices were able to exhibit a similar range of W_{min} values as foams despite having T_{min} values that are up to an order of magnitude lower. Solid materials, on the other hand, exhibited impact absorption efficiencies that are 1 to 3 orders of magnitude worse, although their T_{min} values are low.

These results show that the microlattices presented in this study were able to combine high impact absorption efficiencies with an ultrathin form factor, extending their performance beyond the boundaries of conventional materials. We expect that the impact absorption properties of microlattices could be further improved with a systematic optimization of their designs and selection of the constitutive material.

Fig.15. (a) Experimental data points and calculated trend line (dashed line) of k/k_{bulk} vs. n. (b) Experimental data points and calculated trend line (dashed line) of $\sigma_{c1}/\sigma_{c1,b}$ vs. n. Error bars in (a) and (b) represent the uncertainty due to noise in the measurements. (c) Experimental plot of energy absorbed per unit volume, Q, against nominal stress for microlattices with different n. The dotted line represents the points where maximum impact

absorption efficiency can be achieved.

Fig.16. (a) C_{min} vs. T_{min} and (b) W_{min} vs. T_{min} for the threshold stress range of electronics (i.e. 0.1 MPa ≤ σ ≤ 10 MPa). The alternative materials were silicone rubber [9–11] (pink), polycarbonate [12] (pink), polypropylene foam [5] (green), closed cell polyurethane foam [6] (dark orange), open cell polyurethane foam [1,2] (light orange) and carbon nanotube foam [23] (dark blue). The gray areas indicate the possible theoretical combinations of material thickness and shock absorption performance for current materials. (For interpretation of the references to colour in this figure legend, the reader is referred to the web version of this article.)

6. Conclusions

The dynamic mechanical properties of ultrathin microlattices based on a highly porous 3-D simple cubic design were investigated at high strain rates. It was found that the microlattices were generally crushed layer by layer. The failure of a lattice layer was initiated by buckling for the stretch-dominated design, and plastic yielding for the bending-dominated designs. Further compression led to a sideways deformation of the failing lattice layers, which prevented the auxetic microlattices from compacting at low strains, and contributed to the higher impact absorption efficiencies observed in the microlattices.

In addition, it was found that microlattices subjected to bending-dominated deformation had a lower stiffness and failure strength

compared to the stretch-dominated design, but the lattice layers were less likely to fracture during the crushing process. The net effect of this was an improvement in the energy absorption characteristics of the lattice when its geometry incorporated a slight bending design. For bending-dominated microlattices with higher relative densities, the greater amount of material in the microlattices led to greater lattice stiffness, failure strength and impact energy absorption. These micro-lattices also exhibited similar improvements in their mechanical char-acteristics when they contained a large number of unit cells. More cells minimized the influence of the softer and weaker edge and corner subunit cells, as well as the weakening effects arising from the pre-mature adoption of the secondary deformation mode by non-failing lattice layers. The insights presented here are valid for cases involving

quasistatic and low strain rate loading as well, since the microlattices were under stress equilibrium for the majority of the impact process, and static equations were utilized in the analysis and modelling of the results.

In summary, the microlattice designs proposed in this present study were experimentally shown to reconcile high impact absorption efficiencies with low manufacturable thicknesses in a manner that current materials could not. Furthermore, by utilizing geometrical modifications and size effects, the mechanical properties of the microlattices could be modulated over a meaningful range without altering their relative densities, a trait that is not easily achievable with conventional, stochastic foams. These results indicate that microlattices with designs based on the simple cubic system are potential candidates for ultrathin impact absorbers.

Acknowledgements

Author information

The manuscript was written through the contributions of all authors.

Supporting information available

The supporting information provides additional results and derivations of the equations used in the main text.

Supplementary materials

Supplementary material associated with this article can be found, in the online version, at doi:10.1016/j.ijimpeng.2018.05.014.

References

[1] Rogers Corporation. Handheld shock control design guide 2012.
[2] Rogers Corporation. Material selection guide for portable electronics 2012.
[3] Ye Y, Shi Y, Saw LH, Tay AAO. Performance assessment and optimization of a heat pipe thermal management system for fast charging lithium ion battery packs. Int J Heat Mass Transfer 2016;92:893–903. http://dx.doi.org/10.1016/j.ijheatmasstransfer.2015.09.052.
[4] Ashby MF. The properties of foams and lattices. Philos Trans R Soc Lond Math Phys Eng Sci 2006;364:15–30. http://dx.doi.org/10.1098/rsta.2005.1678.
[5] Bouix R, Viot P, Lataillade J-L. Polypropylene foam behaviour under dynamic loadings: strain rate, density and microstructure effects. Int J Impact Eng 2009;36:329–42. http://dx.doi.org/10.1016/j.ijimpeng.2007.11.007.
[6] Chen W, Lu F, Winfree N. High-strain-rate compressive behavior of a rigid polyurethane foam with various densities. Exp Mech 2002;42:65–73. http://dx.doi.org/10.1007/BF02411053.
[7] Gibson LJ, Ashby MF. Cellular solids: structure and properties. 2 edition Cambridge: Cambridge University Press; 1999.
[8] Notario B, Pinto J, Rodriguez-Perez MA. Nanoporous polymeric materials: a new class of materials with enhanced properties. Prog Mater Sci 2016;78:93–139. http://dx.doi.org/10.1016/j.pmatsci.2016.02.002.
[9] Wacker Chemie A.G. Ultrathin silicone film for high-precision solutions 2014.
[10] Shergold OA, Fleck NA, Radford D. The uniaxial stress versus strain response of pig skin and silicone rubber at low and high strain rates. Int J Impact Eng 2006;32:1384–402. http://dx.doi.org/10.1016/j.ijimpeng.2004.11.010.
[11] Shergold OA, Fleck NA. Experimental investigation into the deep penetration of soft solids by sharp and blunt punches, with application to the piercing of skin. J Biomech Eng 2005;127:838–48.
[12] Dwivedi A, Bradley J, Casem D. Mechanical response of polycarbonate with strength model fits. Army Research Laboratory; 2012.
[13] Bauer J, Hengsbach S, Tesari I, Schwaiger R, Kraft O. High-strength cellular ceramic composites with 3D microarchitecture. Proc Natl Acad Sci 2014;111:2453–8. http://dx.doi.org/10.1073/pnas.1315147111.
[14] Bauer J, Schroer A, Schwaiger R, Kraft O. Approaching theoretical strength in glassy carbon nanolattices. Nat Mater 2016;15:438–43. http://dx.doi.org/10.1038/nmat4561.
[15] Meza LR, Das S, Greer JR. Strong, lightweight, and recoverable three-dimensional ceramic nanolattices. Science 2014;345:1322–6. http://dx.doi.org/10.1126/science.1255908.
[16] Meza LR, Zelhofer AJ, Clarke N, Mateos AJ, Kochmann DM, Greer JR. Resilient 3D hierarchical architected metamaterials. Proc Natl Acad Sci 2015;112:11502–7. http://dx.doi.org/10.1073/pnas.1509120112.
[17] Zheng X, Lee H, Weisgraber TH, Shusteff M, DeOtte J, Duoss EB, et al. Ultralight, ultrastiff mechanical metamaterials. Science 2014;344:1373–7. http://dx.doi.org/10.1126/science.1252291.
[18] Bertoldi K, Reis PM, Willshaw S, Mullin T. Negative poisson's ratio behavior induced by an elastic instability. Adv Mater 2010;22:361–6. http://dx.doi.org/10.1002/adma.200901956.
[19] Ghaedizadeh A, Shen J, Ren X, Xie YM. Tuning the performance of metallic auxetic metamaterials by using buckling and plasticity. Materials 2016;9:54. http://dx.doi.org/10.3390/ma9010054.
[20] Onck PR, Andrews EW, Gibson LJ. Size effects in ductile cellular solids. Part I: modeling. Int J Mech Sci 2001;43:681–99. http://dx.doi.org/10.1016/S0020-7403(00)00042-4.
[21] Andrews EW, Gioux G, Onck P, Gibson LJ. Size effects in ductile cellular solids. Part II: experimental results. Int J Mech Sci 2001;43:701–13. http://dx.doi.org/10.1016/S0020-7403(00)00043-6.
[22] Thevamaran R, Daraio C. An experimental technique for the dynamic characterization of soft complex materials. Exp Mech 2014;54:1319–28.
[23] Thevamaran R, Meshot ER, Daraio C. Shock formation and rate effects in impacted carbon nanotube foams. Carbon 2015;84:390–8. http://dx.doi.org/10.1016/j.carbon.2014.12.006.
[24] Thevamaran R, Raney JR, Daraio C. Rate-sensitive strain localization and impact response of carbon nanotube foams with microscale heterogeneous bands. Carbon 2016;101:184–90. http://dx.doi.org/10.1016/j.carbon.2015.12.069.
[25] Merkt S, Hinke C, Bültmann J, Brandt M, Xie YM. Mechanical response of TiAl6V4 lattice structures manufactured by selective laser melting in quasistatic and dynamic compression tests. J Laser Appl 2014;27:S17006. http://dx.doi.org/10.2351/1.4898835.
[26] Jindal UC. Machine design. Pearson Education India; 2010.
[27] Wang CM, Wang CY. Exact solutions for buckling of structural members. 1 edition Boca Raton, FL: CRC Press; 2004.
[28] Bastawros A-F, Bart-Smith H, Evans AG. Experimental analysis of deformation mechanisms in a closed-cell aluminum alloy foam. J Mech Phys Solids 2000;48:301–22. http://dx.doi.org/10.1016/S0022-5096(99)00035-6.
[29] Kanahashi H, Mukai T, Nieh TG, Aizawa T, Higashi K. Effect of cell size on the dynamic compressive properties of open-celled aluminum foams. Mater Trans 2002;43:2548–53. http://dx.doi.org/10.2320/matertrans.43.2548.
[30] Yamada Y, Wen CE, Shimojima K, Mabuchi M, Nakamura M, Asahina T, et al. Effects of cell geometry on the compressive properties of nickel foams. Mater Trans 2000;41:1136–8.
[31] Nayak NC, Tripathy DK. Deformation and energy absorption characteristics of microcellular ethylene-octene copolymer vulcanizates. Polym Eng Sci 2002;42:1274–85. http://dx.doi.org/10.1002/pen.11030.
[32] Misra A, Raney JR, De Nardo L, Craig AE, Daraio C. Synthesis and characterization of carbon nanotube–polymer multilayer structures. ACS Nano 2011;5:7713–21. http://dx.doi.org/10.1021/nn202262j.